Supplementary Materials for

Perirhinal input to neocortical layer 1 controls learning

Guy Doron*†, Jiyun N. Shin†, Naoya Takahashi, Moritz Drüke, Christina Bocklisch, Salina Skenderi, Lisa de Mont, Maria Toumazou, Julia Ledderose, Michael Brecht, Richard Naud, and Matthew E. Larkum*
†These authors contributed equally to this work

Correspondence to: matthew.larkum@hu-berlin.de and guydoron@gmail.com

This PDF file includes:

Materials and Methods

Animals

All experiments and procedures were approved and conducted in accordance with the guidelines given by Landesamt für Gesundheit und Soziales Berlin (G0278/16). The following animal lines were used in this study: C57BL/6J wild-type mice, Gpr26-cre transgenic mice (18, 19), SST::ChR2 transgenic mice (SST-IRES-Cre mice (JAX stock #018973) crossed with Ai32 mice (JAX stock #024109) (51), Rbp4-cre transgenic mice (26) and Wistar rats (Charles River). Male animals were used except for two Rbp4-cre female mice for two-photon dendritic imaging. The animals were housed in reversed 12 h light/dark cycle (light on between 21:00 and 09:00) and all the behavioral experiments were performed during the dark period of the cycle.

Retrograde tracing and analysis

Wistar rats and C57BL/6J mice (>2 weeks old) were anesthetized under ketamine/xylazine (13 mg kg^{-1} / 1mg kg^{-1} for mice, 100 mg kg^{-1} / 5 mg kg^{-1} for rats, intraperitoneal (i.p.) injection) before head-fixed at the stereotaxic frame. Animals were kept on a thermal blanket during entire surgery and recovery. After incision of the scalp, skull was cleaned with 70% ethanol and a craniotomy over the barrel field of S1 (Mice: 1 mm x 1 mm, centered at anterior-posterior axis (AP) -1 mm, medial-lateral axis (ML) 3.25 mm; Rats: 2 mm x 2 mm, centered at AP -2.5 mm, ML 5.5 mm) was made on the basis of stereotaxic coordinates. Retrograde tracer, Fast Blue (1% in dH2O, Polysciences), was soaked in a sterile piece of tissue and then applied onto the surface of S1 for 5 min for mice and 10 min for rats. Seven days later, animals were perfused transcardially with phosphate-buffered saline (PBS) followed by 4% paraformaldehyde (PFA) and the brain was extracted. 100 µm-(mice) or 150 µm-(rats) thick coronal brain sections were made using a vibratome (Leica VT1000S, Leica Biosystems) and mounted on slide glasses with synthetic mounting medium (ROTI Mount, Carl Roth). Fast Blue labelled cells in the perirhinal cortex were detected manually under an epifluorescent microscope (Leica DMI4000 B, Leica Biosystems). These areas were identified based on stereotaxic coordinates (53, 54). The number of counted cells in each coronal section was normalized by the total number of counted cells per brain.

Anterograde tracing and analysis

For anterograde tracing and optogenetic *ex-vivo* experiments AAV1.hSyn.hChR2(H134R)-EYFP.WPRE.hGH (Penn Vector Core) was injected in the perirhinal cortex of >2 weeks old C57BL/6J mice and Wistar rats. Anesthesia was induced and maintained with isoflurane at 5% and 2%, respectively for mice. Rats were under anesthesia with ketamine/xylazine (100 mg kg^{-1} / 5 mg kg^{-1} for rats, i.p.). Animals were kept on a thermal blanket during entire surgery and recovery. Animals were placed in a stereotaxic frame and craniotomies were performed based on stereotaxic coordinates: AP -1.8 mm, ML ± 4.1 mm, DV -4.2 mm from bregma for mice / AP -3.8 mm, ML ± 6.0 mm, DV -7.0 mm from bregma for rats. Injections were carried out using graduated pipettes broken back to a tip diameter of 10-15 µm, at a rate of ~25 nl/min for a total volume of 50-70 nl (mice) or 100 nl (rats). Incubation time was at least 3 weeks before transcradial perfusion or *ex-vivo* experiment.

AAV1.hSyn.hChR2(H134R)-EYFP.WPRE.hGH containing acute brain sections were imaged using an Olympus BX51 Microscope with a 4x objective. Fluorescence intensity was quantified with ImageJ software by plotting a line profile across the cortical layers that calculates the brightness value. The average gray value of each images was normalized by subtracting the minimum intensity of each section (baseline) and dividing with maximum intensity of each section.

Ex-vivo electrophysiology

After 3-4 weeks of virus expression, sagittal or coronal slices (300 µm thick) were prepared from 35-50 day old C57BL/6J mice. Whole-cell patch-clamp recordings were performed from visually identified L5 pyramidal neurons and L1 interneurons using infrared Dodt-gradient contrast video microscopy. The extracellular solution contained 125 mM NaCl, 25 mM NaHCO3, 25 mM Glucose, 3 mM KCl, 1.25 mM NaH2PO4, 2 mM CaCl2, 1 mM MgCl2, pH 7.4 at ~33 º C. The intracellular solution contained 115 mM K+-gluconate, 20 mM KCl, 2 mM Mg-ATP, 2 mM Na2-ATP, 10 mM Na2-phosphocreatine, 0.3 mM GTP, 10 mM HEPES, 0.05 mM Alexa 594 and biocytin (0.2%), pH 7.2. Whole-cell voltage recordings were performed from the soma (4-6 MΩ) using a Multiclamp 700b

(Molecular devices) amplifier. Data was acquired with an ITC-18 board and analyzed using Igor software. Optogenetic synaptic stimulation was performed via an LED (470 nm) (2 ms pulses) located in L1 around the tuft dendrite. To activate hM4Di receptor, Clozapine-N-Oxide (CNO) (Tocris Bioscience) was bath applied (final concentration 10 µM).

Chemogenetic manipulation of perirhinal axonal activity

Mice (>4 weeks) were anesthetized with ketamine/xylazine (13 mg kg^{-1} / 1mg kg^{-1}, i.p.) and kept on a thermal blanket during entire surgery and recovery. Lidocaine (1%, wt/vol, AlleMan Pharma) was injected around the surgical site before the scalp incision. The periosteum was removed and small craniotomy was made on the injection sites. Injection coordinates for the perirhinal cortex were AP -1.8 mm, ML ±4.2 mm, DV -4.2 mm and for POm were AP -2 mm, ML +1.2 mm, DV -3.0 mm from bregma. AAV1/2-hSyn1-hM4D(Gi)-mCherry-WPRE-hGHp(A) (Viral Vector Facility of the University of Zurich) was injected bilaterally except for n=2 mice with unilateral injection in the perirhinal cortex of the right hemisphere (0.15 – 0.20 µl per side). The behavioral training started after >2 weeks of expression.

In order to activate hM4Di receptor, CNO dissolved in extracellular solution (final concentration 10 µM) was back-loaded in a glass pipette and applied into L1 (150 µm) of S1 by gentle pressure at least 20 min before the microstimulation training. CNO was applied into two adjacent sites (150 µl each) of the craniotomy to maximize the CNO diffusion area.

Estimation of DREADD effect on cortical layers

First to quantify the spread of CNO across cortical layers, 0.5% Chicago Sky Blue 6B (Sigma-Aldrich) diluted in ringer solution was back loaded in a glass pipette and applied with gentle pressure in L1 (150 µm) of S1, where CNO was applied. Then mice were sacrificed and the brain was extracted before post-incubation in 4% PFA for >24 hours. Coronal brain sections were made using a vibratome (Leica VT1000S, Leica Biosystems) and mounted on slide glasses with DAPI-containing mounting medium (ROTI Mount FluorCare DAPI). Then brain sections were imaged under an epifluorescent microscope (Leica DMI4000 B, Leica Biosystems).

Fluorescence intensity was quantified with ImageJ software by plotting a line profile across the cortical layers with a bin size of 2.594 μm. The average gray value of each images was then normalized by subtracting the minimum intensity of each section and dividing with maximum intensity of each section. Average intensity of Chicago Sky Blue was convolved with the average intensity of EYFP in perirhinal axons in S1 measured from anterograde tracing to calculate the estimated effect of DREADD manipulation as a function of cortical depths. Then layer boundaries were marked based on Lefort et al., 2009 (52). The effect of DREADD on each layer was computed by calculating the area under the curve between layer boundaries divided by the total area under the curve.

Quantification of DREADD expression

hM4Di-mCherry fluorescence intensity was quantified with ImageJ software by plotting a line profile, across 1000 μm above and below from the rhinal fissure with a bin size of 2.594 μm. The average gray value of each image was then normalized by subtracting the minimum intensity of each section and dividing by the intensity at the rhinal fissure of each section. The boundaries of the perirhinal cortex was defined as 250 μm above and 750 μm below the rhinal fissure based on stereotaxic coordinates (53). Expression rate was calculated by measuring area under the curve within the perirhinal cortex or outside the perirhinal cortex divided by the total area under the curve.

Headpost implant and head-restraint habituation

A lightweight aluminum head-post (mouse) or a metal bolt (rat) was implanted on the skull of the animal under ketamine/xylazine anaesthesia (13 mg kg^{-1} / 1mg kg^{-1} for mice, 100 mg kg^{-1} / 5 mg kg^{-1} for rats, i.p.). For mice used in chemogenetic experiments, the implantation was performed >10 days after viral injection. After the scalp and periosteum were removed, a thin layer of light curing adhesives (OptiBond, Kerr and Charisma, Kulzer) was applied to the skull. A head-post was fixed on the skull on the left hemisphere with a dental cement (Paladur, Heraeus Kulzer).

Head-restraint habituation began >3 days after the head-post implantation. Habituation time at the first day was 5 min and then gradually increased each day until the animal sat calmly for 1 h. Animals were water restricted from the second day (1 ml/day)

of the habituation and then trained to receive the saccharin (Sigma-Aldrich) water (0.5% for mice and 0.1% for rats) from the licking port from the fourth day of the habituation. Licking was monitored using a piezo-based sensor attached to the licking port. Weight and health of the animal were monitored daily. Habituation for head restraint and licking typically took 5 days.

Two to three days before the microstimulation training or/and juxtacellular recording, 1.5 mm x 1.5 mm craniotomy was made on the right barrel cortex centered at AP -1.25 mm and ML +3.25 mm from bregma for mice and 2 mm x 2 mm craniotomy centered at AP -2.5 mm and ML +5.5 mm from bregma was made for rats. For juxtacellular recordings in the rat perirhinal cortex, 2 mm x 2 mm craniotomy was made on AP -4.5 mm and ML +5.0 mm from bregma. Then a recording chamber was implanted for chronic access to this region. The dura was left intact and the craniotomy was covered with silicon (Kwik-Cast, World Precision Instruments).

Microstimulation detection task

Animals were trained to perform the microstimulation task as described elsewhere (13, 42). Briefly, animals were trained to respond with tongue lick to a 200 ms train of microstimulation pulses applied to barrel cortex (40 cathodal pulses at 200Hz, 0.3 ms pulse duration) through a tungsten microelectrode (Microprobes) in depth of ~700 μm (mice) or ~1500 μm (rats) from pia. Inter-stimulus interval was randomly distributed by Poisson delay with time constant 3 s. In the first session, initial intensity of 160 μA pulses were injected into the cortex and coupled with a drop of water reward (pairing period). After five pairing trials, testing periods began where animals were rewarded only if they licked the licking port within 100 to 1,200 ms (response window) after stimulus onset. Tongue lick responses were detected with piezo-based sensors (mice) or beam breaker (rats). The time of the first lick after stimulus onset was taken as the reaction time. Trials with reaction time between 0.1 s to 1.2 s from the stimulus onset were counted as hits and trials with no lick or reaction time longer than 1.2 s were counted as misses. When animals licked prematurely within 0.1 s from stimulus onset, that trial was aborted. To encourage animals to use a non-conservative response criterion, we only mildly punished licks in the inter-stimulus interval with an additional 1.5 s delay to the next stimulus presentation. Once

animals reached 80% hit rate, pulse intensity was gradually decreased during and over the sessions until it reached the target intensity of 10 μA (mice) or 5 μA (rats). The number of total trials were not fixed per session but a session was terminated either when animals stopped licking to free water presentation or when they reached the intensity threshold, which was defined as the lowest intensity with hit rate ≥ 80%. Control animals reached to the target intensity within 3-5 days of training. We define expert animals as animals that performed the task with ≥ 80% hit rate at the target intensity. Untrained animals received μStim at the target intensity (10 μA for mice and 5 μA for rats) without any pairing trial.

Behavioral quantification

The performance of the animals during μStim task was quantified by computing cumulative difference of the number of hit trials and the number of miss trials. We define the cumulative value at the last trials as learning score (i.e. number of total hit trials – number of total miss trials). Since the learning score compares the number of hit trials and the number of miss trials, it is dependent on the total number of trials. As described above the total number of trials per session was not fixed. To compensate for the various total number of trials per animal, we normalized the learning score with the total number of trials, resulting in a value ranging from -1 to 1. Negative values indicate higher number of miss trials than hit trials while positive values indicate that hit number was greater than miss trials.

Pharmacology

To inhibit neuronal activity in the hippocampus and perirhinal cortex, a glass pipette was filled with lidocaine (AlleMan Pharma; 1%, wt/vol) and inserted into the ipsilateral hippocampus or perirhinal cortex based on stereotaxic coordinates (53, 54). The drug (150 nl) was injected by a gentle pressure at least 20 min before the training onset. To inhibit Ca^{2+} spikes in apical dendrites, 100 μM baclofen was applied 3 min prior to the training at a depth of 150 μm in S1. Injections (150 nl each) was made every 20 min throughout the training.

Optogenetic manipulations

For optogenetic activation of Somatostatin-positive (SST) neurons, SST::ChR2 transgenic mice expressing ChR2 in SST-positive cells were used. Photostimulation light (465 nm, 2 mW; Doric Lenses Inc) with 500-ms pulse starting at 300 ms before stimulus onset was delivered via the optic fiber placed above the craniotomy. To prevent the mice from responding to the light rather than to µStim, the recording chamber was covered with a black rubber to prevent light leakage from photostimulation into the animals' eyes.

In vivo juxtacellular recording and analysis

Following head-restraint habituation, juxtacellular recordings were performed from deep layer neurons from S1 and the perirhinal cortex in awake head-fixed animals during µStim detection task. For experiments in Fig.2, control mice that did not express hM4Di receptors were also treated with CNO in L1 of S1 in order to exclude the indirect effect of CNO on neuronal activity (16). The glass pipette (4–8 MΩ) for juxtacellular recording during microstimulation task was filled with extracellular solution containing: 135 mM NaCl, 5.4 mM KCl, 1.0 mM MgCl2, 1.8 mM CaCl2 and 5 mM HEPES (pH 7.2). The juxtacellular signal was amplified and low-pass filtered at 3 kHz by a patch-clamp amplifier (NPI) and sampled at 25 kHz by a Power1401 data acquisition interface under the control of Spike2 software (CED). For perirhinal recording in rats, the pipette was inserted with 17° toward lateral and 50° toward anterior. The mean depth in juxtacellular recordings are following: S1 in mice: 1145.0±19.15 mm, S1 in rats: 1462±25.41 mm, perirhinal cortex in rats: 6339.64 ±122.07 mm, which is likely an overestimate of the true depth due to oblique penetrations and dimpling.

Recorded neurons were separated into putative fast-spiking (FS) interneurons and regular-spiking (RS) pyramidal neurons based on spike half-width and firing rate. Cells with spike half-width lower than 0.5 ms and firing rate higher than 8 Hz were classified to FS. Only RS were used for further analysis.

All the cells and trials recorded over days were pooled together for comparing activity (firing rate or burst rate) changes during µStim trials. Bursts were identified as at least two spikes with an inter-spike interval of ≤15 ms. Burst rates were calculated by dividing the number of total burst events with the length of the time window (event/s). For the analysis in Fig. 2, the time window between 1 and 0 s before the stimulus ([-1, 0] s) was used to

calculate the baseline activity and 0.2–2.5 s ([+0.2, +2.5] s) after the stimulus was used to calculate post-stimulus activity. Spikes could not be reliably detected during the μStim period ([0, +0.2] s) due to electric artifacts caused by μStim. For firing rate and burst rate change analysis in perirhinal recordings, the difference between pre-stimulus frequency and post-stimulus frequency was divided by average pre-stimulus frequency.

For z-score normalization, peri-stimulus time histograms (PSTHs) were computed for each cell with a bin size of 50 ms and the stationary rate and standard deviation were computed based on the baseline PSTHs. Z-score of cells with no spikes during the baseline period could not be computed and not shown in Fig. 2 and 3. Z-score of burst rate was computed in the same manner but using PSTHs based on burst rate instead of firing rate. PSTHs in the post-stimulus period were used to define significantly modulated cells in Fig. 2. For multiple comparisons, p-value of 0.05 was corrected by Bonferroni method and converted to z-score (z=3.267 for 46 bins). Bins with z-score higher than Bonferroni corrected z-score was considered as significantly modulated bins. Cells with at least one significantly modulated bin were defined as modulated cells. For burst rate, cells having spikes but no bursts during the baseline period were classified as non-modulated cells.

For the classification of L5 neurons in expert animals (Fig. 3), PSTHs were calculated for each cell by averaging spikes in time bins of 100 ms for times within 2 seconds of hit-trials. For each cell, the stationary rate and standard deviation (SD) were computed based on the PSTHs in the period [-2, 0] s. Cells were classified to ON cell or OFF cell if PSTHs in the period [0.3, 0.4] s was either more than 3* SD above the stationary rate, or less than 3*SD below, respectively. Other cells were classified as NR cells.

Two-photon Ca^{2+} imaging and analysis

For dendritic Ca^{2+} imaging, AAV2/1-Syn-Flex-GCaMP6s-WPRE.SV40 (Addgene) was injected through a glass pipette (tip diameter, 5–10 μm) into the left S1 barrel cortex of adult Rbp4-Cre mice (#031125-UCD, MMRRC) on the basis of stereotaxic coordinates (AP -1.5 mm and ML 3.2 mm from bregma). A single injection (100 nl) was made at 700 μm deep from the pial surface. Three weeks after the injection, a 3-mm craniotomy was made over the injection site and sealed with a 3-mm glass coverslip (#1) with cyanoacrylate glue. A light-weight head-post was fixed on the skull in the right hemisphere with light-

curing adhesives and a dental cement. Habituation of mice to head restraint and following imaging experiment began 4 weeks after the virus injection.

Imaging from behaving mice was performed with a resonant-scanning two-photon microscope (Thorlabs) equipped with GaAsP photomultiplier tubes (Hamamatsu Photonics). GCaMP6s was excited at 940 nm (typically 30–40 mW at the sample) with a Ti:Sapphire laser (Mai Tai eHP Deep See, Spectra-Physics) and imaged through a 16×, 0.8 NA water immersion objective (Nikon). Full-frame images (256 × 256 pixels, 175 × 175 μm2) were acquired from apical dendrites of L5 neurons expressing GCaMP6s at a depth of 150–200 μm at 58.6 Hz using ScanImage 4.1 software (Vidrio Technologies). Tungsten electrodes for microstimulation were inserted through the access port on the chronic glass window.

For axonal calcium imaging, AAV2/1-Syn-GCaMP6s-WPRE (Addgene) was into the bilateral perirhinal cortex of adult C57BL/6J mice on the basis of stereotaxic coordinates (AP -1.8 mm, ML ±4.2 mm and DV -4.2 mm from bregma). Three weeks after the injection, a 3-mm chronic glass window was implanted over the left S1. Images (512×512 pixels, 133×133 μm2) were acquired from GCaMP6s-expressing axonal fibers in L1 (at a depth of 30–40 μm) at 30.3 Hz. For each mouse, imaging was performed in the same field of view with the same laser power throughout the experimental period.

All analysis for Ca^{2+} imaging was performed using custom-written scripts in MATLAB (MathWorks). Horizontal and vertical drifts of imaging frames due to animal motion were corrected by registering each frame to a reference image based on whole-frame cross-correlation. The reference image was generated by averaging any given consecutive 100 frames in which motion drifts were minimal. Regions of interest (ROIs) for apical dendrites of L5 neurons were manually selected with the help of average intensity and standard deviation projections across movie frames. For each ROI, pixel values inside the ROI were averaged to obtain the time series of Ca^{2+} fluorescence. The extracted signals were corrected for neuropil contamination by subtracting the local, peri-dendritic neuropil signals. For axonal imaging, axonal Ca^{2+} signals were extracted from field ROIs (~100 × 100 μm2). Fluorescence change (ΔF/F0) was calculated as $(F - F_0)/F_0$, where F0 was the baseline fluorescence value in the ROI throughout the whole imaging session.

For the classification of dendrites, PSTHs were calculated for each dendrite by averaging Ca^{2+} responses in hit trials. For each dendrite, the baseline fluctuation, i.e., SD, was computed from the PSTH in the period [-1, 0] s. Dendrites were classified to ON dendrites or OFF dendrites if the PSTHs in the period [0, 2] s was either more than 3*SD above the baseline, or less than 3*SD below, respectively. Other dendrites were classified as NR dendrites.

Single-Neuron Stimulation Detection Task

Once rats performed at current intensities below 5 μA on 2 consecutive days, we switched to single-cell stimulation experiments, as previously described (13, 42). Briefly, the animals were head fixed during the task, and waited for the microstimulation/nanostimulation detection task to begin, which occured when a neuron was found. The glass pipette for juxtacellular single-cell stimulation and recording was glued to a tungsten microelectrode used for microstimulation at a distance of ~70 mm, as described elsewhere (13, 42). The glass pipette was filled with intracellular solution containing: 135 mM K-gluconate; 10 mM HEPES; 10 mM Na2-phosphocreatine; 4 mM KCl; 4 mM MgATP; and 0.3 mM Na3GTP (pH 7.2). Recording depth was 1902.0.6±63.12 mm, which is likely an overestimate of the true depth due to oblique penetrations and dimpling.

During single-cell stimulation trials, a fixed duration square-wave current pulse was injected into a neuron through a glass pipette. Every stimulation sequence contained each step exactly once, while their order was varied pseudo-randomly from trial to trial. To induce a regular spike pattern, we used a single 100 ms DC current step. To elicit a burst like spike pattern, brief stimulation duration of 25 ms was used, followed by 1175 ms inhibition at current intensities of 50% used in the nanostimulation, to prevent any further spikes during the stimulation trial. Single-cell stimulation trials, catch trials without current injection and microstimulation trials were pseudo randomly interleaved in a series of 6 trials including 3 microstimulation trials, 2 single-cell stimulation trials (each of different duration) and 1 catch trial. All trials were presented at random intervals (Poisson process, mean 3 s). Microstimulation currents were adjusted (range 3-8 μA, mean 4.2 ± 1.1 μA (standard deviation)) such that animals performed close to the detection threshold, resulting

in an average microstimulation hit rate of 90%. Only cells with all three types of stimulation trials were included.

Statistics

All statistics were performed using MATLAB (MathWorks). Unless otherwise stated, all values are indicated as mean ± standard error mean (SEM). Statistical significance was determined using Wilcoxon sign-rank test within group and Wilcoxon rank-sum test between groups at a significance level of 0.05. For comparing proportions, chi-square test was performed. For non-parametric multiple comparisons, Kruskal-Wallis test was followed by post-hoc Dunn-Sidàk test, when applicable. For comparison of hit rates and false-positive rates in nanostimulation experiment, one-sided t-test was performed. No statistical tests were run to predetermine sample size, and blinding and randomization were not performed.

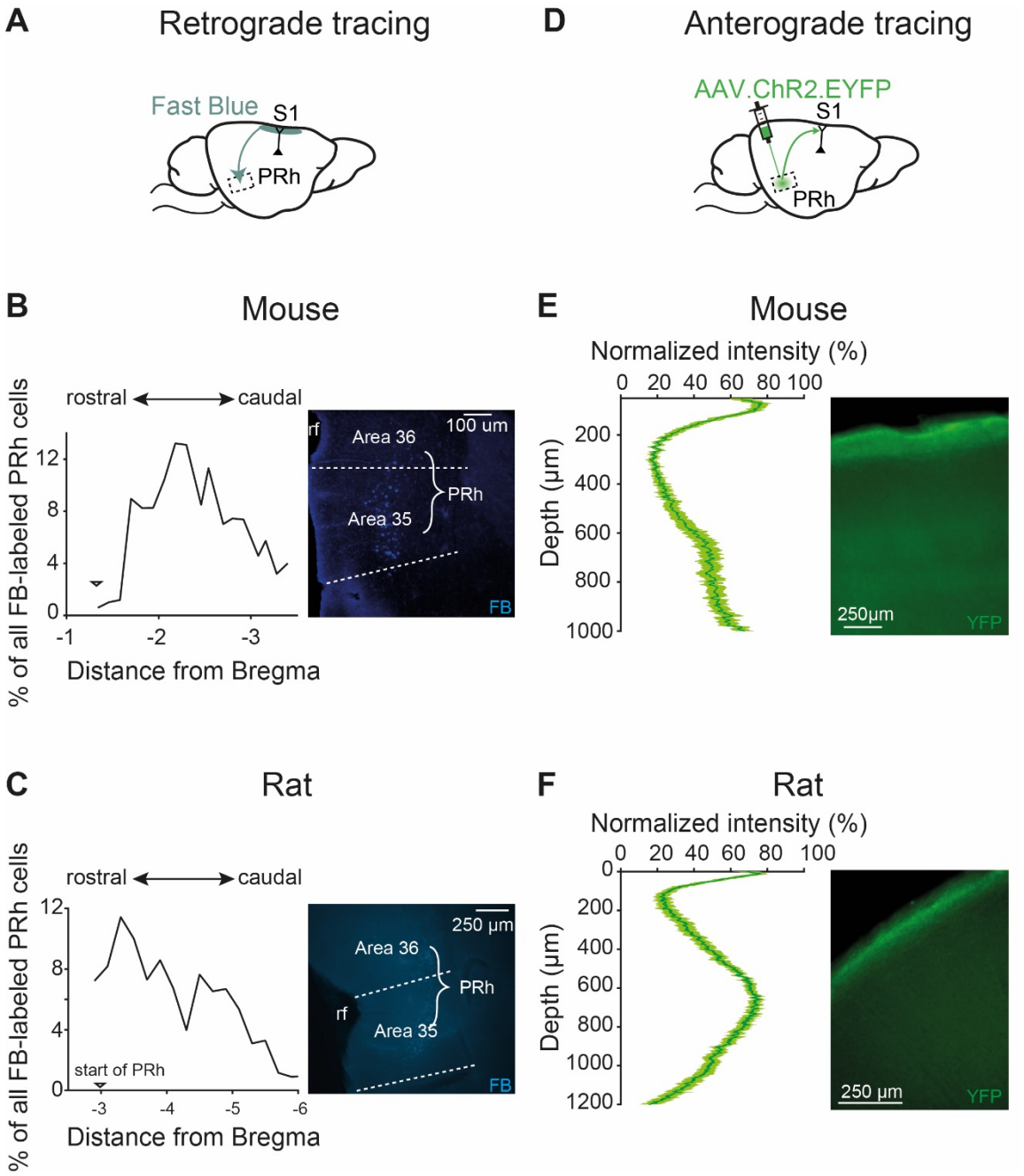

Fig. S1. Quantification of retrograde and anterograde tracing.

(A) Schematic of retrograde tracing. Fast Blue (FB) was applied to L1 of S1. **(B), (C)** Rostro-caudal distribution of FB-labelled cells in mouse PRh (n=6 brains) and rat PRh (n=2 brains), respectively. PRh starts (marked by arrows) from -1.3 mm and -3 mm from bregma in mice and rats, respectively. **(D)** Schematic of anterograde tracing.

AAV.EYFP.ChR2 was injected into PRh. **(E), (F)** Normalized YFP fluorescent intensity across cortical layers in mouse S1 (n=20 brain sections) and rat S1 (n=16 brain sections).

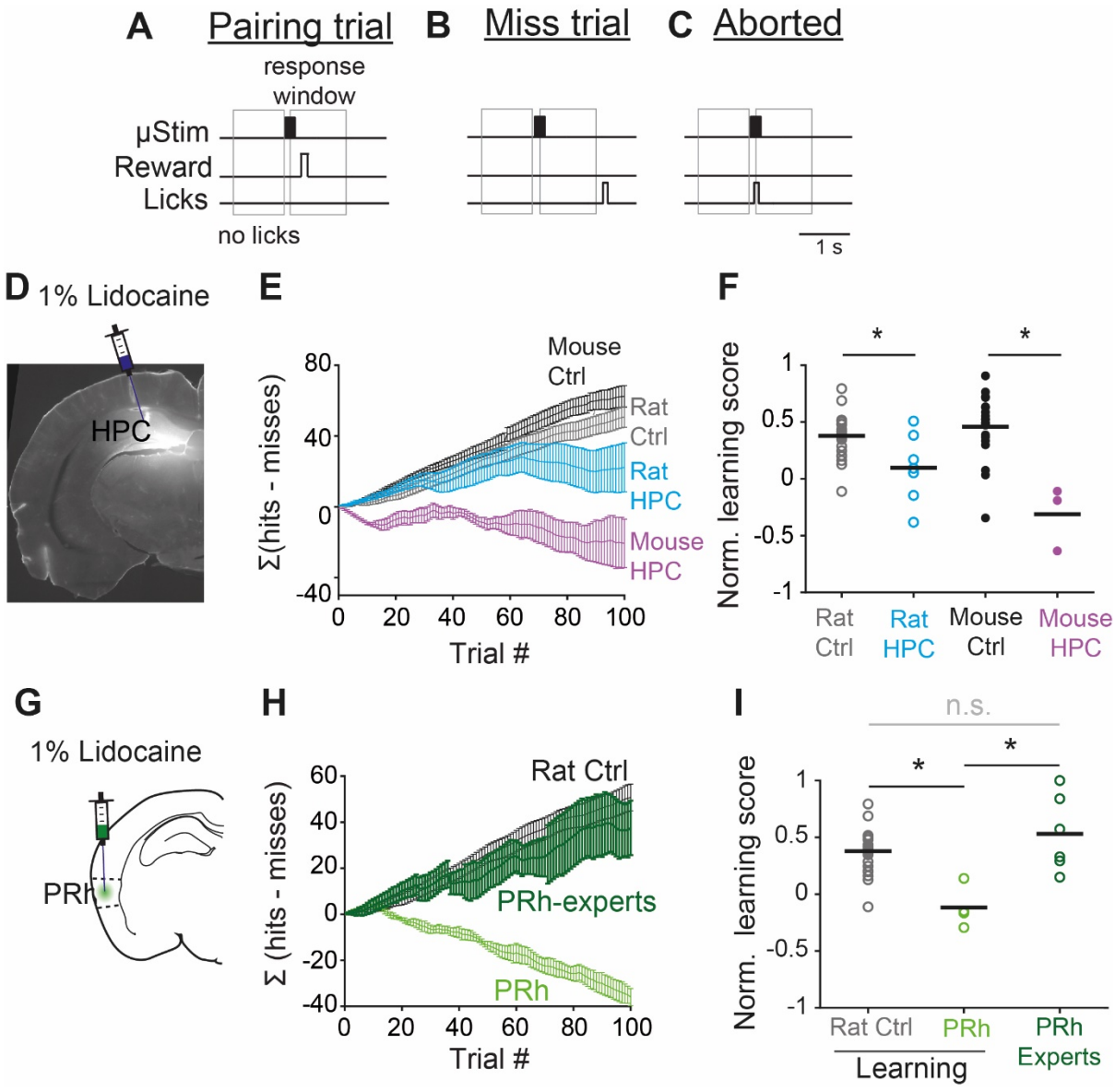

Fig. S2. Microstimulation detection task depends on the hippocampus and perirhinal cortex.

(A) During the paring period, water reward was coupled with µStim regardless of the animal's licking response. **(B)** When animals did not lick or licked outside the response window upon µStim (Miss), water reward was not given. **(C)** Premature licking (<0.1 ms from µStim onset) aborted the trial. Water reward was not given in these trials. **(D)** To inhibit neuronal activity in the hippocampus, 1% lidocaine was injected before the onset of µStim training. The image shows the spread of Chicago Sky Blue injected in the same area. **(E)** Cumulative learning curve of control mice (n=20, black), control rats (n=24, gray),

HPC lidocaine-injected mice (n=3, purple) and HPC lidocaine-injected rats (n=7, light blue) during the first session. **(F)** Normalized learning score of control rats (0.38±0.04, n=24), HPC lidocaine-injected rats (0.03±0.16, n=7), control mice (0.46±0.06, n=20) and HPC lidocaine-treated mice (-0.31±0.16, n=3) at the first session. Each dot corresponds to individual animals and black line indicates mean. Wilcoxon rank-sum test, rat Ctrl vs. rat HPC, *p=0.02, mouse Ctrl vs. mouse HPC, *p=0.01. **(G)** Schematic of lidocaine injection in PRh. **(H)** Cumulative learning curve of control rats (n=31, gray), PRh lidocaine-injected rats during learning (PRh, n=4, light green) and PRh lidocaine-injected rats after learning (PRh-experts, n=6, dark green). **(I)** Normalized learning score of control rats (0.38±0.04, n=24), PRh lidocaine-treated rats (-0.12±0.09, n=4) and PRh trained (0.53±0.14, n=6). Each dot corresponds to individual rats and black line indicates mean. Kruskal-Wallis test, p=0.007, post-hoc Dunn-Sidàk test, Rat Ctrl vs. PRh, *p=0.01, Rat Ctrl vs. PRh-experts, n.s. p=0.9, PRh vs. PRh-experts, *p=0.01.

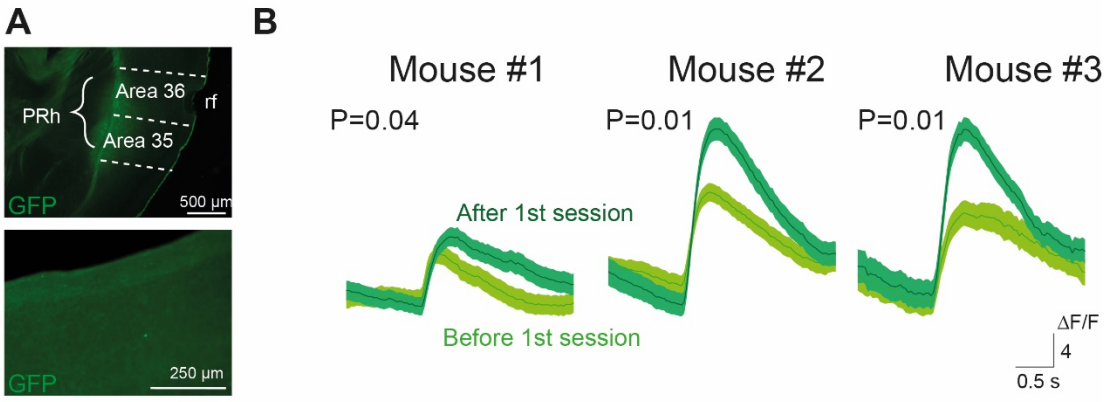

Fig. S3. Calcium activity in perirhinal axons in L1 of S1.

(A) GCaMP6s expression in PRh (upper) and GFP-expressing axons in L1 of S1 (lower). **(B)** Axonal calcium transients in three mice before and after the first session (Mouse #1, n=61 trials before 1st session, n=60 trials after 1st session; mouse #2, n=102 trials, n=62 trials after 1st session, mouse#3, n=64 trials before 1st session, n=63 trials after 1st session). Calcium responses were significantly enhanced in all three mice when compared individually. P-values are from Wilcoxon rank-sum test.

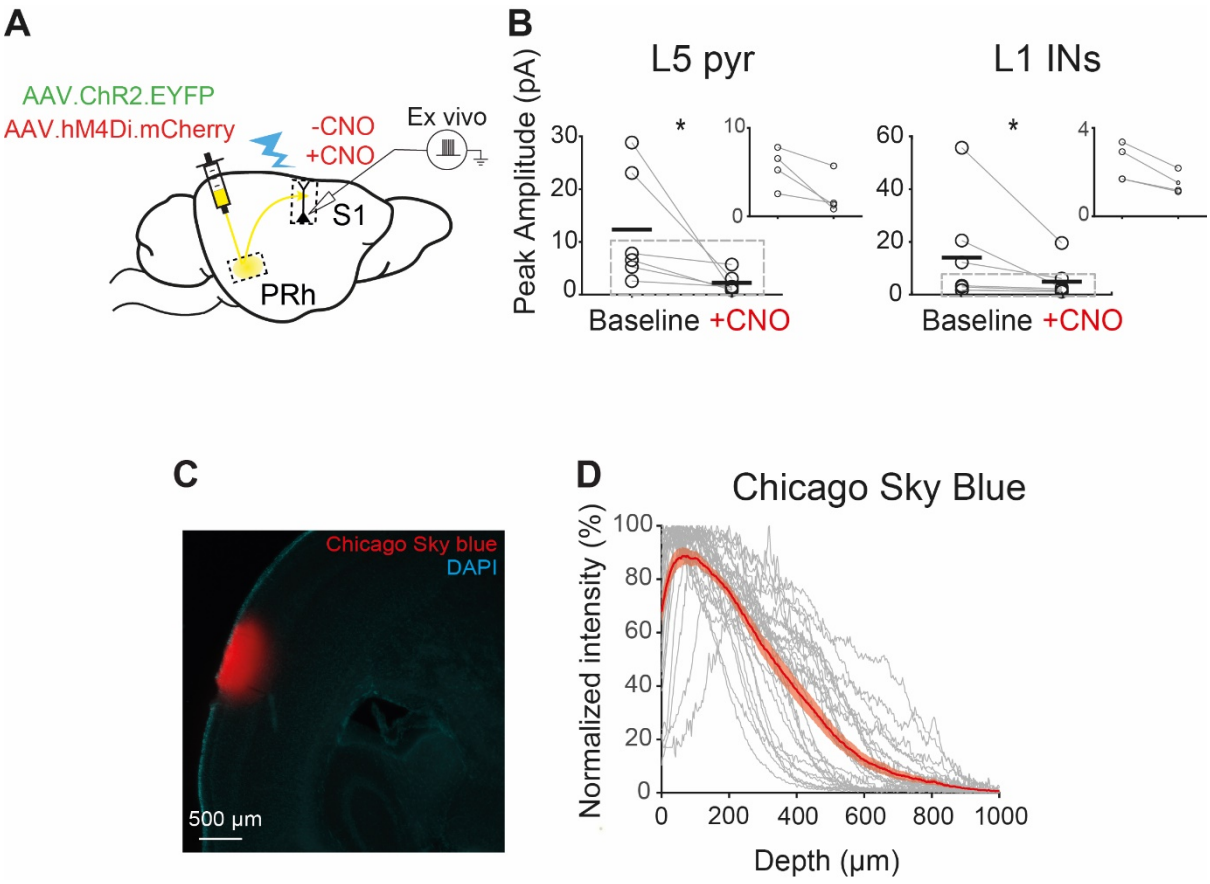

Fig. S4. Validating the efficacy of DREADD suppression.

(A) Schematic of *ex-vivo* experiments. AAV.ChR2.EYFP and AAV.hM4Di.mCherry were co-injected in PRh *in vivo*. After >3 weeks of incubation, whole-cell recording was performed in *ex-vivo* brain slices during optogenetic activation of ChR2 with and without CNO. **(B)** Same dataset as Fig. 1E but compared separately for L5 pyramidal neurons (baseline 12.34±4.43 pA vs. +CNO 2.23±0.77 pA, n=6, Wilcoxon sign rank test, *p=0.03) and L1 interneurons (baseline 14.01±7.43 pA vs. +CNO 4.90±2.53 pA, n=7, Wilcoxon sign-rank test, *p=0.016). Light-evoked EPSC amplitudes were significantly reduced after CNO application in both cell classes. Black lines indicate the mean. Inset, enlarged view of the dotted box. **(C)** Spread of CNO was estimated by injecting Chicago Sky Blue at the same depth in S1. Image shows the fluorescent signal of Chicago Sky blue. **(D)** Quantification of fluorescent intensity across cortical layers. Gray lines show normalized

intensity in each brain section (n=29 sections from n=7 injections) and the red line indicates the average normalized intensity and SEM.

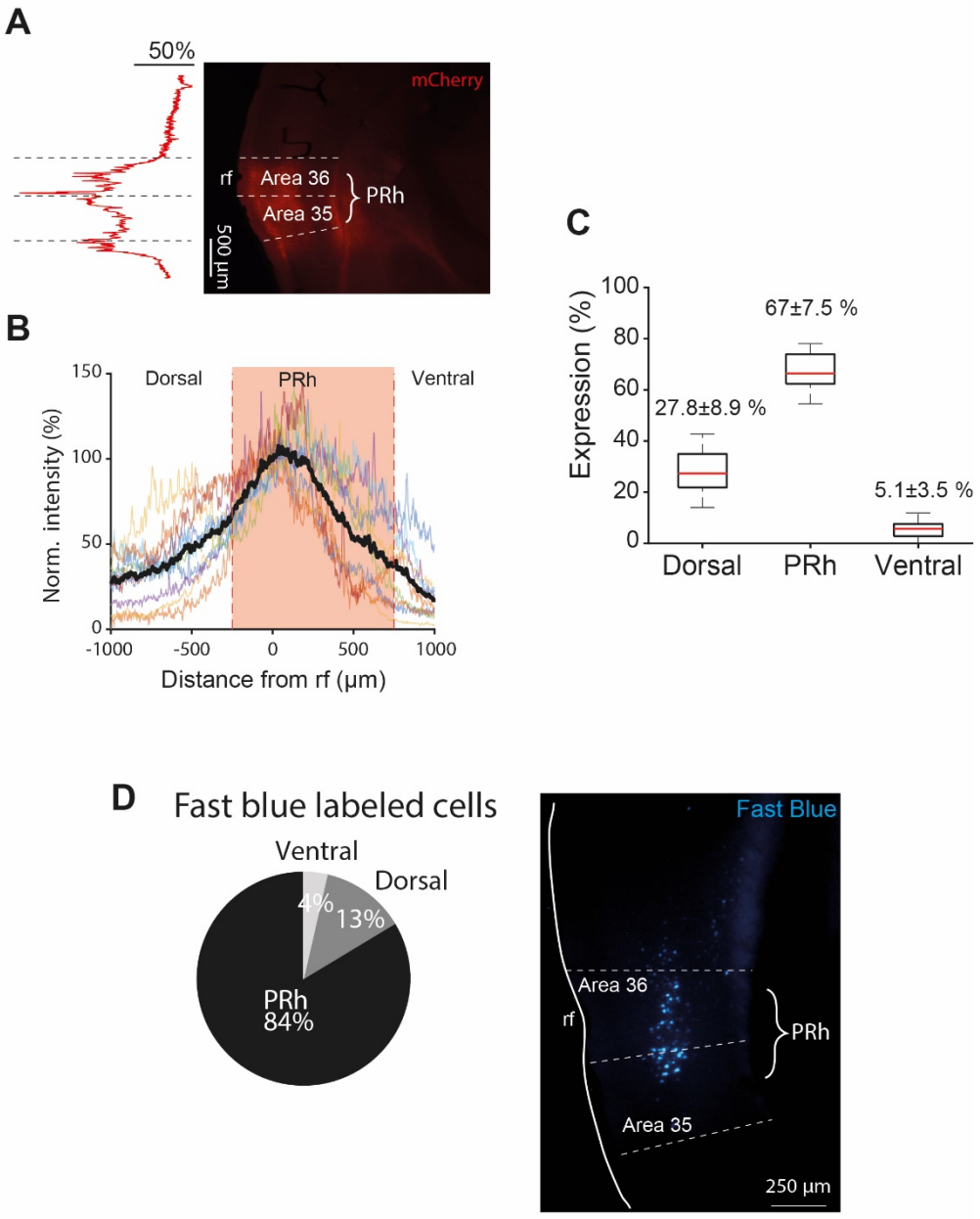

Fig. S5. Specificity of hM4Di expression.

(A) hM4Di expression around PRh was quantified by measuring mCherry fluorescent intensity (see Methods). Example trace of normalized fluorescent intensity and the corresponding epifluorescent image. **(B)** Normalized mCherry expression between 1000 µm dorsal and 1000 µm ventral from the rhinal fissure, which marks the location of PRh. Colored lines show normalized fluorescence intensity from brains of each mice (n=11) used in this study. Black line shows the mean. Red box indicates the PRh. **(C)**

Quantification of mCherry expression in PRh and neighboring areas (see Methods). Most of the expression was observed in PRh (67%) but there was a small leakage into neighboring areas, especially in dorsal areas (28%). Numbers show mean ± standard deviation. **(D)** Quantification of FB-labelled cells in PRh and neighboring areas. In order to quantify how many neurons in areas neighboring PRh project to L1 of S1, we counted Fast blue (FB)-labeled neurons in the same areas as in **(B-C)** and found that majority of neurons (84%) that project to L1 of S1 comes from PRh. Taken together, these results suggest that our DREADD manipulation was highly specific to perirhinal neurons that project to L1 of S1.

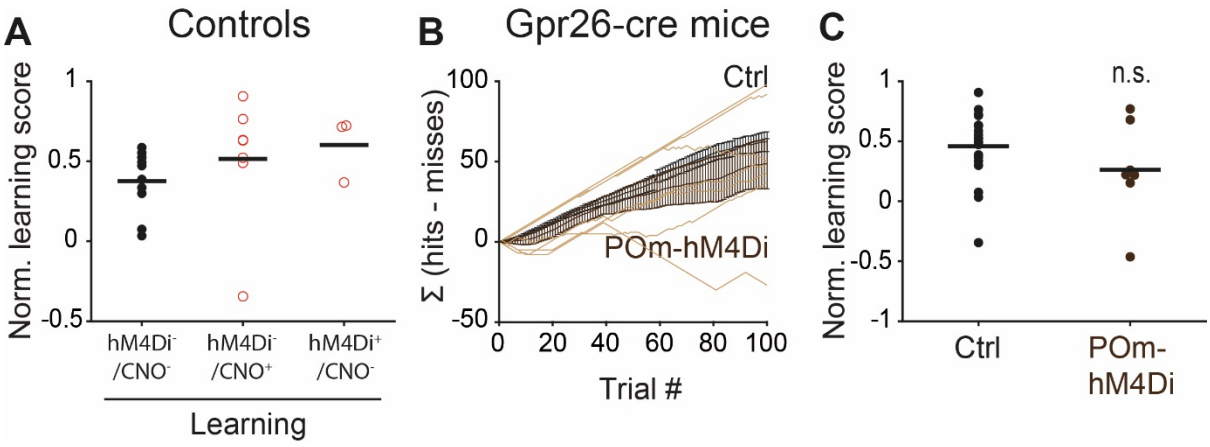

Fig. S6. Controls for DREADD manipulation.

(A) Normalized learning score of different controls for DREADD. Both CNO control group (hM4Di-/CNO+, 0.51±0.15, n=7 mice) and hM4Di control group (hM4Di+/CNO-, 0.60±0.11, n=3 mice) showed similar level of learning measured by learning score compared to wild-type group (hM4Di-/CNO-, 0.38±0.06, n=10 mice). Kruskal-Walis test, p=0.12. **(B)** Cumulative learning curve of control mice (black) and mice with suppression of POm axons in L1 of S1 (POm-hM4Di, brown) during the first session. **(C)** Normalized learning score of control mice (0.46±0.06, n=20) and POm-hM4Di mice (0.26±0.15, n=7) at the first session. Each dot corresponds to individual mice and black line indicates mean. Wilcoxon rank-sum test, n.s. p=0.13.

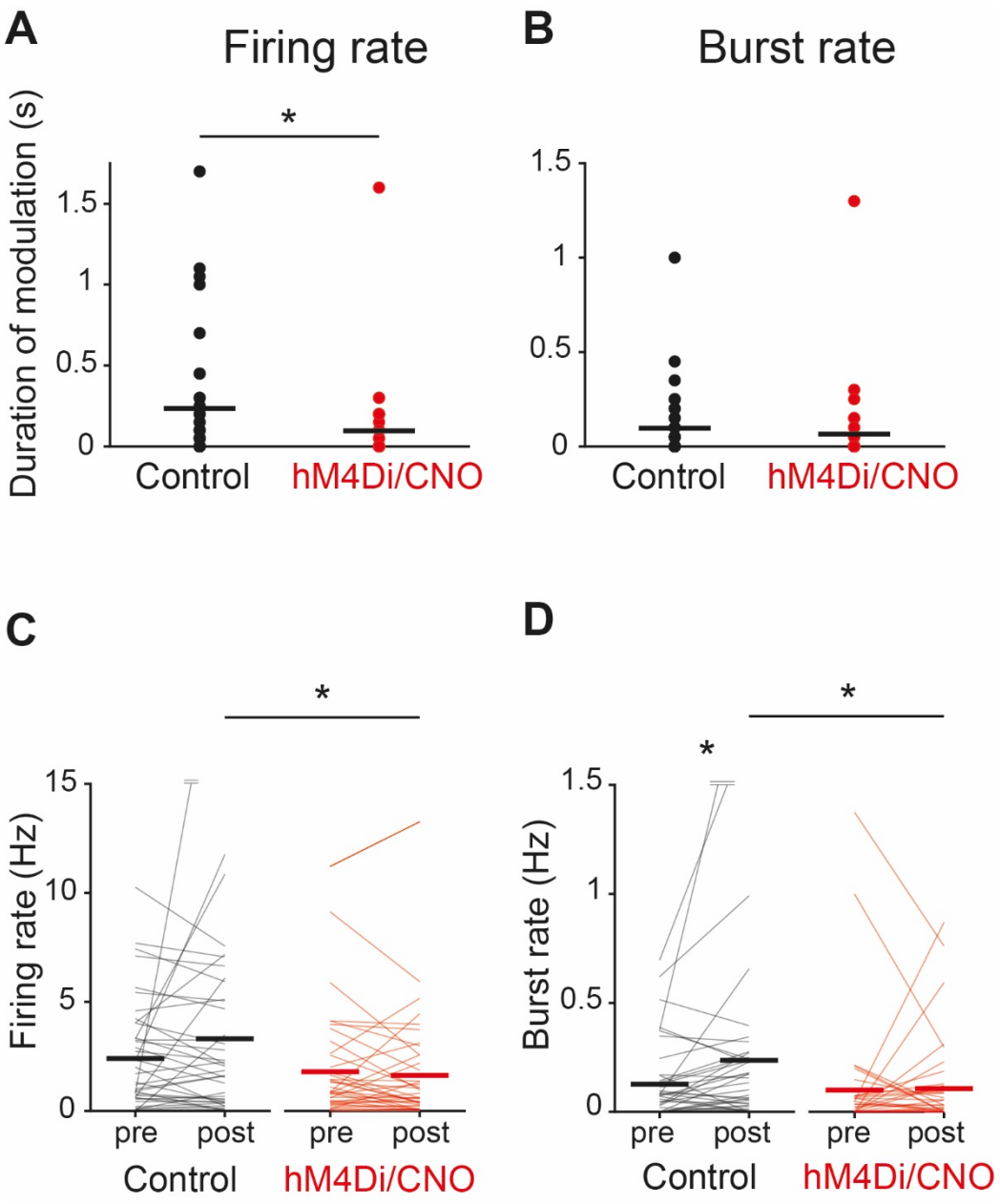

Fig. S7. PRh inputs to L1 modulates activity of L5 pyramidal neurons during learning.

(A) Duration of modulated activity measured as number of 50 ms time bins following stimulus presentation where firing rate was significantly different to baseline in control (235±64 ms) and hM4Di/CNO mice (94±45 ms). Wilcoxon rank-sum test, *p=0.01. **(B)** Same as **(A)** for burst rate in control (95±31 ms) and hM4Di/CNO mice (65±37 ms), respectively. Wilcoxon rank-sum test, *p=0.03. **(C), (D)** Population averaged firing rate

and burst rate of L5 pyramidal neurons during µStim learning in control and hM4Di/CNO S1, respectively. Firing rate: Control, pre-stimulus 2.40±0.39 Hz vs. post-stimulus 3.31±0.69 Hz, n=42 neurons, Wilcoxon sign-rank test, p=0.69; hM4Di/CNO, pre-stimulus 1.79±0.38 Hz vs. post-stimulus 1.63±0.39 Hz, n=41 neurons, Wilcoxon sign-rank test, p=0.28. Burst rate: Control, pre-stimulus 0.13±0.03 Hz vs. post-stimulus 0.24±0.07 Hz, Wilcoxon sign-rank test, *p=0.03; hM4Di/CNO, pre-stimulus 0.10±0.04 Hz vs. post-stimulus 0.11±0.03 Hz, Wilcoxon sign-rank test, p=0.75. Control post-stimulus vs. hM4Di post-stimulus: firing rate, Wilcoxon rank-sum test, *p=0.04; burst rate, Wilcoxon rank-sum test, *p=0.04.

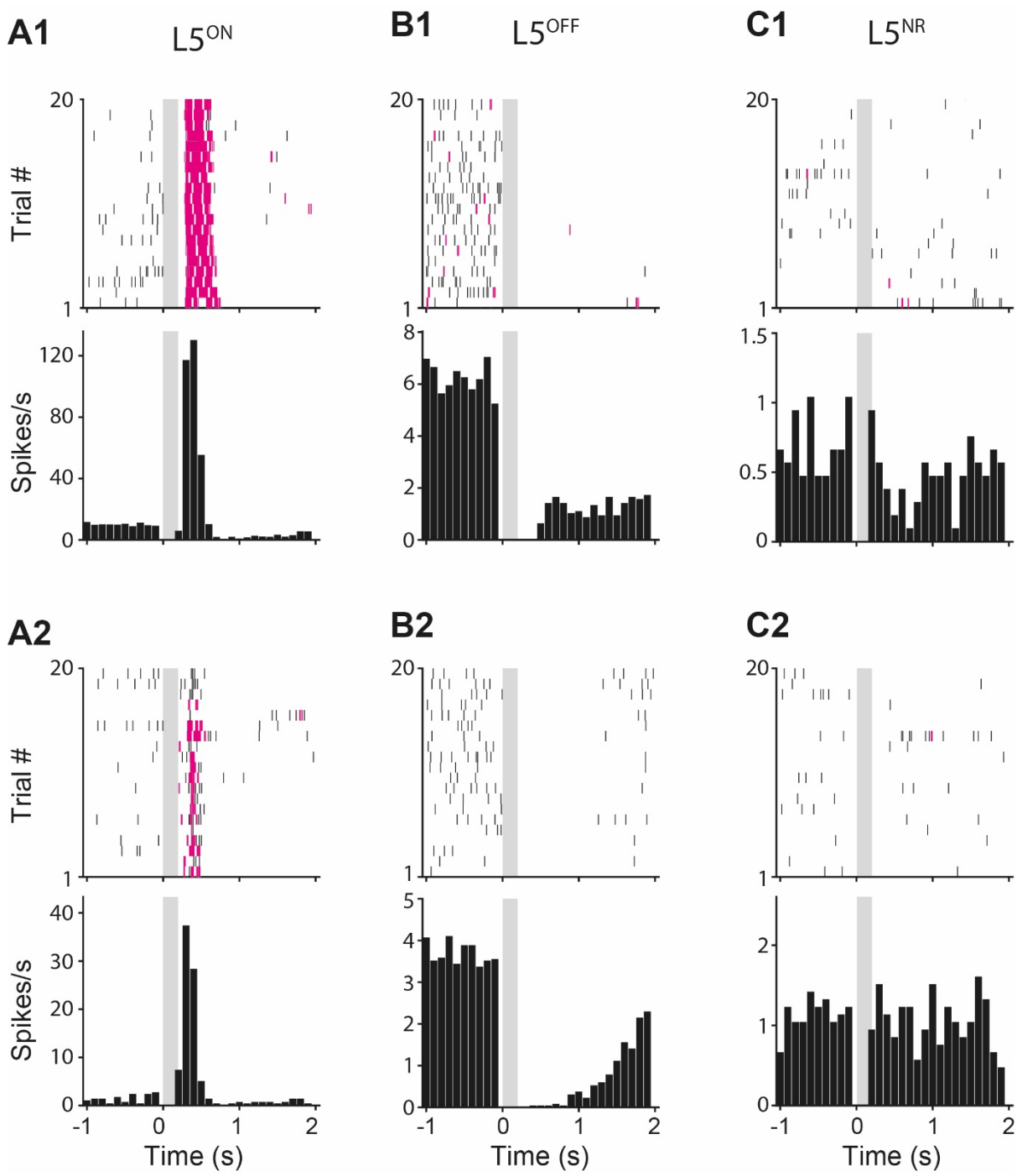

Fig. S8. Example responses of L5^{ON}, L5^{OFF} and L5^{NR} neurons.

(A1-A2) Raster plots (upper) and PSTHs of two example L5^{ON} neurons in experts during µStim task. **(B1-B2)** Same for L5^{OFF} neurons. **(C1-C2)** Same for L5^{NR} neurons. Bursts are marked by pink ticks in raster plots. Gray bar: µStim. Note that y-axis in PSTHs differ for visibility.

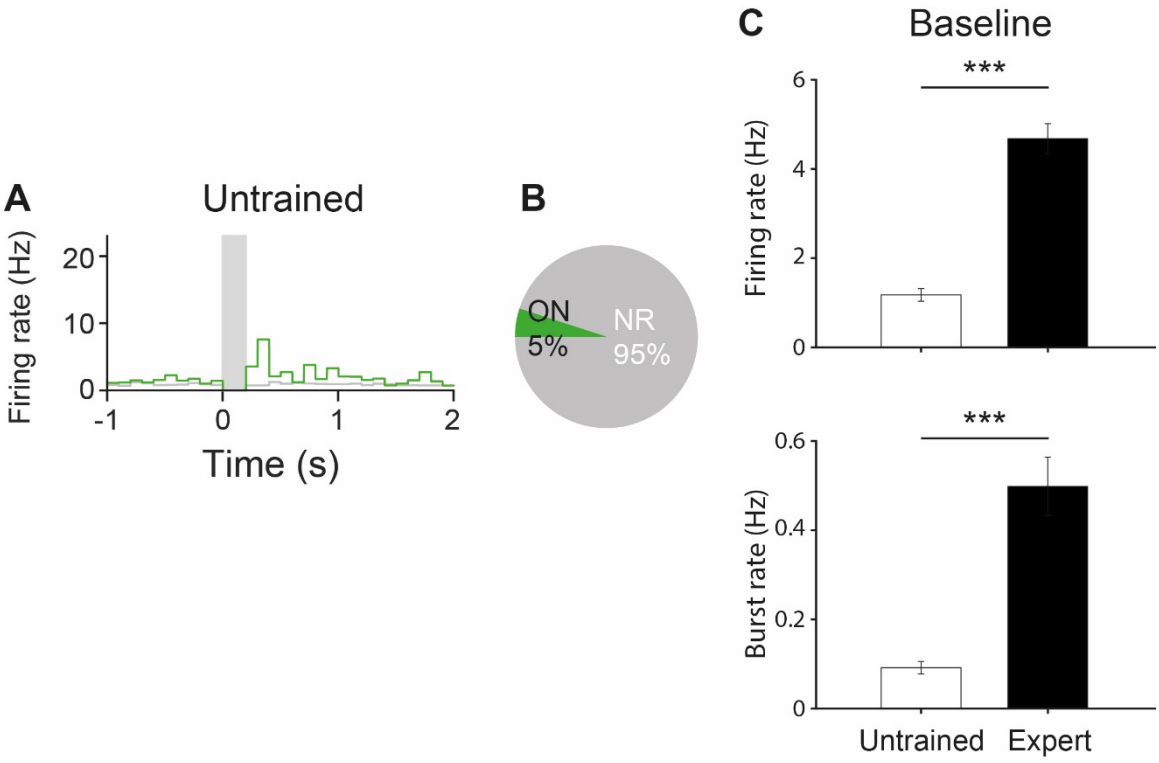

Fig. S9. Lack of distinctive three L5 subpopulations in untrained rats.

(A) Average PSTHs of $L5^{ON}$ and $L5^{NR}$ neurons in untrained rats. Gray box: µStim. **(B)** Fraction of $L5^{ON}$ and $L5^{NR}$ neurons in untrained rats (total n=66 cells). There was no cell classified to $L5^{OFF}$ cells. **(C)** Average baseline activity of L5 pyramidal neurons in S1 of untrained (n=66 cells) and expert rats (n=273 cells). Firing rate: untrained 1.18±0.14 vs. experts 4.68±0.34 Hz, Wilcoxon rank-sum test, ***$p<0.001$; Burst rate: untrained 0.09±0.01 Hz vs. experts 0.50±0.07 Hz, Wilcoxon rank-sum test, ***$p<0.001$.

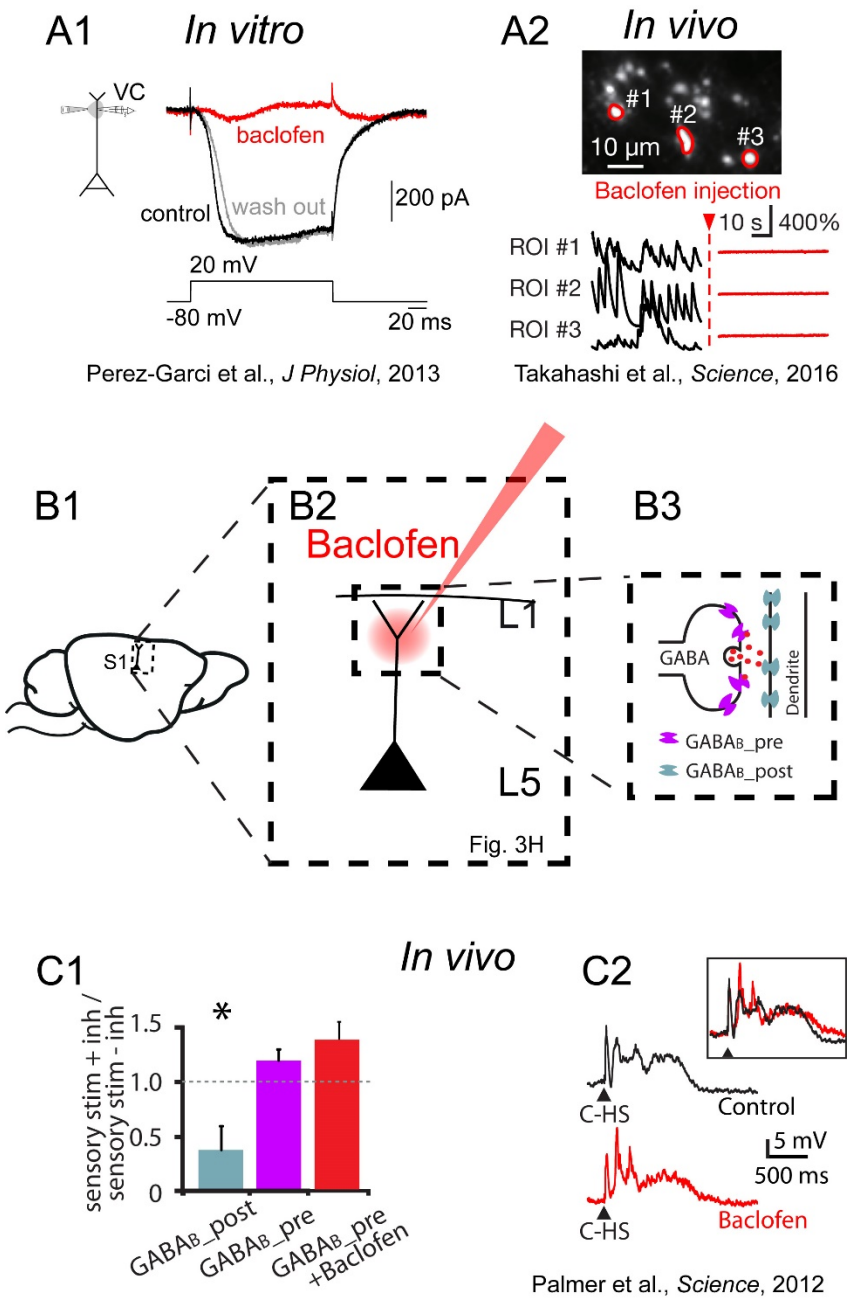

Fig. S10. Extended discussion of the likelihood that a dendritic mechanism is involved in µstim-induced behavioral plasticity.

At present, it is very difficult to block regenerative dendritic events (e.g. dendritic Ca^{2+} spikes) in awake behaving animals without interfering with other important mechanisms such as synaptic transmission. Fig. 3H-J shows two approaches providing evidence for a putative dendritic mechanism underlying the µStim detection task learning: a) the activation of dendrite-targeting SST inhibitory neurons and b) the local application

of baclofen to the cortex, both of which blocked learning similarly to blocking perirhinal input to L1. In addition to these experiments, there were circumstantial reasons to suspect a dendritic mechanism:

1) The activity of L5 pyramidal neurons was modulated by perirhinal input to L1, for which the most parsimonious explanation would be some effect on the tuft dendrites that innervate L1 (Fig. 2).

2) There was a shift to increased burst-spiking in L5 pyramidal neurons during perirhinal-dependent learning (Figs. 2&3) and burst firing has been shown to be induced by dendritic activity (*20*).

3) The distribution of L5 firing responses corresponded closely to the subpopulations of L5 dendrites on the basis of their dendritic Ca^{2+} activity (Fig. 3).

Nevertheless, it is important for a reader to be aware that none of these lines of evidence, nor their combination, are definitive evidence for the dendritic location of the mechanism for plasticity involved in μStim-induced learning.

Local application of baclofen – can it be used to selectively block regenerative dendritic Ca^{2+} events in order to test their contribution?

We provide here a roadmap to understanding the action of baclofen in suppressing dendritic activity. Local application of baclofen, a $GABA_B$ receptor agonist, has proven surprisingly effective in blocking dendritic Ca^{2+} spikes in vitro (*30, 31*) and in vivo (*24, 32, 33*). This is because dendritic $GABA_B$ receptors activate hyperpolarizing Kir3-type K^+ channels (*55*) and completely block dendritic L-type Ca2+ currents necessary for dendritic Ca^{2+} spikes (A1; *31*). Consistent with the in vitro data, two-photon imaging in awake behaving rodents also showed that local perfusion of baclofen completely abolished both spontaneous and evoked Ca^{2+} transients in the apical dendrites (A2; *24*) which we presume is also the case in this study (B1-2).

The most important caveat to take into account when using baclofen to block dendritic activity is that $GABA_B$ receptors are also associated with presynaptic inhibition at many axon terminals in the brain (*56*). We have addressed this issue in a previous study using transgenic animals selectively expressing $GABA_B$ receptor isoforms known to be pre- and post-synaptically located (B3; purple and light blue respectively). Here, we showed that sensory stimuli that evoked $GABA_B$-mediated dendritic inhibition (interhemispheric

inhibition) only occurred in mice with postsynaptic $GABA_B$ receptors but not mice that only had presynaptic $GABA_B$ receptors (C1; *32*). Moreover, baclofen had no effect in mice with only presynaptic $GABA_B$ receptors, suggesting that this inhibition was mediated by postsynaptic $GABA_B$ receptors and that presynaptic inhibition did not play any role in interhemispheric (i.e. long-range evoked) inhibition. In the same study, we also showed that subthreshold input to L5 pyramidal neurons was unaffected by local perfusion of baclofen suggesting that network activity influencing L5 neurons was not substantially affected by baclofen acting on presynaptic sites (C2).

In summary, the remarkably effective block of dendritic Ca^{2+} activity following activation of dendritic $GABA_B$ receptors with baclofen and its minimal influence on presynaptic inhibition, suggest that for certain questions baclofen can be an effective tool for selectively suppressing dendritic Ca^{2+} activity. However, better tools need to be developed to definitively isolate the contribution of dendritic Ca^{2+} activity in behavior.

Figures modified from originals with permission.

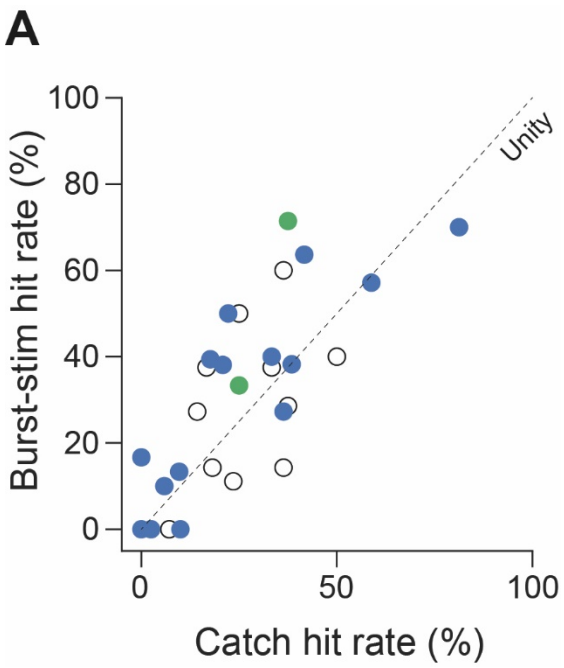

Fig. S11. Three cell-response classes of nanostimulation cells.

(A) Nanostimulation cells were classified by the same criteria used for Fig. 3. Green dots indicate $L5^{ON}$ cells (n=2 out of 28 cells), blue dots indicate $L5^{OFF}$ cells (n=15 out of 28 cells) and black empty dots indicate $L5^{NR}$ cells (11 out of 28 cells). Cells inducing higher hit rate to burst trials than to catch trials include all of the three cell classes.

REFERENCES AND NOTES

1. H. Eichenbaum, A cortical–hippocampal system for declarative memory. Nat. Rev. Neurosci. 1, 41–50 (2000).

2. E. T. Rolls, A computational theory of episodic memory formation in the hippocampus. Behav. Brain Res. 215 (2010), pp. 180–196.

3. J. J. Letzkus, S. B. E. Wolff, E. M. M. Meyer, P. Tovote, J. Courtin, C. Herry, A. Lüthi, A disinhibitory microcircuit for associative fear learning in the auditory cortex. Nature. 480, 331–335 (2011).

4. F. Gambino, S. Pagès, V. Kehayas, D. Baptista, R. Tatti, A. Carleton, A. Holtmaat, Sensory-evoked LTP driven by dendritic plateau potentials *in vivo*. Nature. 515, 116–119 (2014).

5. E. Abs, R. B. Poorthuis, D. Apelblat, K.-K. Conzelmann, I. Spiegel, J. J. Letzkus, Learning-Related Plasticity in Dendrite-Targeting Layer 1 Interneurons. Neuron. 100, 684–699 (2018).

6. L. E. Williams, A. Holtmaat, Higher-Order Thalamocortical Inputs Gate Synaptic Long-Term Potentiation via Disinhibition. Neuron. 101, 91-102 (2019).

7. N. L. Xu, M. T. Harnett, S. R. Williams, D. Huber, D. H. O'Connor, K. Svoboda, J. C. Magee, Nonlinear dendritic integration of sensory and motor input during an active sensing task. Nature. 492, 247–251 (2012).

8. J. Cichon, W.-B. Gan, Branch-specific dendritic Ca^{2+} spikes cause persistent synaptic plasticity. Nature. 520, 180–185 (2015).

9. S. Manita, T. Matsumoto, J. Nakai, Y. Yanagawa, M. Odagawa, T. Suzuki, M. E. Larkum, M. Ohkura, A. Yamanaka, K. Ota, M. Sato, C. Homma, K. Yamada, A. Inutsuka, Y. Hayashi, C. Matsubara, M. Murayama, A Top-Down Cortical Circuit for Accurate Sensory Perception. Neuron. 86, 1304–1316 (2015).

10. M. P. Witter, H. J. Groenewegen, Connections of the parahippocampal cortex in the cat. III. Cortical and thalamic efferents. J. Comp. Neurol. 252, 1–31 (1986).

11. K. L. Agster, R. D. Burwell, Cortical efferents of the perirhinal, postrhinal, and entorhinal cortices of the rat. Hippocampus. 19, 1159–1186 (2009).

12. L. R. Squire, C. E. L. Stark, R. E. Clark, THE MEDIAL TEMPORAL LOBE. Annu. Rev. Neurosci. 27, 279–306 (2004).

13. A. R. Houweling, M. Brecht, Behavioural report of single neuron stimulation in somatosensory cortex. Nature. 451, 65–68 (2008).

14. T. J. Stachniak, A. Ghosh, S. M. Sternson, Chemogenetic Synaptic Silencing of Neural Circuits Localizes a Hypothalamus→Midbrain Pathway for Feeding Behavior. Neuron. 82, 797–808 (2014).

15. B. N. Armbruster, X. Li, M. H. Pausch, S. Herlitze, B. L. Roth, Evolving the lock to fit the key to create a family of G protein-coupled receptors potently activated by an inert ligand. Proc. Natl. Acad. Sci. U. S. A. 104, 5163–8 (2007).

16. J. L. Gomez, J. Bonaventura, W. Lesniak, W. B. Mathews, P. Sysa-Shah, L. A. Rodriguez, R. J. Ellis, C. T. Richie, B. K. Harvey, R. F. Dannals, M. G. Pomper, A. Bonci, M. Michaelides, Chemogenetics revealed: DREADD occupancy and activation via converted clozapine. Science. 357 (2017), doi:10.1126/science.aan2475.

17. N. J. Audette, S. M. Bernhard, A. Ray, L. T. Stewart, A. L. Barth, Rapid Plasticity of Higher-Order Thalamocortical Inputs during Sensory Learning. Neuron. 103, 277–291 (2019).

18. T. B. Oram, AhissarE., O. Yizhar, Soc Neuro Abstr, in press.

19. T. A. Zolnik, J. Ledderose, M. Toumazou, T. Trimbuch, T. Oram, C. Rosenmund, B. J. Eickholt, R. N. S. Sachdev, M. E. Larkum, Layer 6b Is Driven by Intracortical Long-Range Projection Neurons. Cell Rep. 30, 3492-3505 (2020).

20. M. E. Larkum, J. J. Zhu, B. Sakmann, A new cellular mechanism for coupling inputs arriving at different cortical layers. Nature. 398, 338–341 (1999).

21. M. E. Larkum, J. J. Zhu, Signaling of layer 1 and whisker-evoked Ca^{2+} and Na^{+} action potentials in distal and terminal dendrites of rat neocortical pyramidal neurons *in vitro* and *in vivo*. J. Neurosci. 22, 6991–7005 (2002).

22. P. Schwindt, W. Crill, Mechanisms Underlying Burst and Regular Spiking Evoked by Dendritic Depolarization in Layer 5 Cortical Pyramidal Neurons. J. Neurophysiol. 81, 1341–1354 (1999).

23. M. E. Larkum, W. Senn, H. R. Lüscher, Top-down dendritic input increases the gain of layer 5 pyramidal neurons. Cereb. Cortex. 14, 1059–1070 (2004).

24. N. Takahashi, T. G. Oertner, P. Hegemann, M. E. Larkum, Active cortical dendrites modulate perception. Science. 354, 1587–1590 (2016).

25. S. R. Williams, G. J. Stuart, Mechanisms and consequences of action potential burst firing in rat neocortical pyramidal neurons. J. Physiol. 521, 467–482 (1999).

26. C. R. Gerfen, R. Paletzki, N. Heintz, GENSAT BAC Cre-Recombinase Driver Lines to Study the Functional Organization of Cerebral Cortical and Basal Ganglia Circuits. Neuron. 80, 1368–1383 (2013).

27. F. Helmchen, K. Svoboda, W. Denk, D. W. Tank, *In vivo* dendritic calcium dynamics in deep-layer cortical pyramidal neurons. Nat. Neurosci. 2, 989–996 (1999).

28. L. Beaulieu-Laroche, E. H. S. Toloza, N. J. Brown, M. T. Harnett, Widespread and Highly Correlated Somato-dendritic Activity in Cortical Layer 5 Neurons. Neuron. 103, 235–241 (2019).

29. V. Francioni, Z. Padamsey, N. L. Rochefort, High and asymmetric somato-dendritic coupling of V1 layer 5 neurons independent of visual stimulation and locomotion. Elife. 8 (2019), doi:10.7554/eLife.49145.

30. E. Pérez-Garci, M. Gassmann, B. Bettler, M. E. Larkum, The $GABA_{B1b}$ Isoform Mediates Long-Lasting Inhibition of Dendritic Ca^{2+} Spikes in Layer 5 Somatosensory Pyramidal Neurons. Neuron. 50, 603–616 (2006).

31. E. Pérez-Garci, M. E. Larkum, T. Nevian, Inhibition of dendritic Ca^{2+} spikes by GABA B receptors in cortical pyramidal neurons is mediated by a direct $G_{i/o}$-βγ-subunit interaction with Ca_{v1} channels. J. Physiol. 591, 1599–1612 (2013).

32. L. M. Palmer, J. M. Schulz, S. C. Murphy, D. Ledergerber, M. Murayama, M. E. Larkum, The Cellular Basis of $GABA_B$-Mediated Interhemispheric Inhibition. Science. 335, 989–993 (2012).

33. M. Suzuki, M. E. Larkum, Dendritic calcium spikes are clearly detectable at the cortical surface. Nat. Commun. 8, 276 (2017).

34. H. Makino, T. Komiyama, Learning enhances the relative impact of top-down processing in the visual cortex. Nat. Neurosci. 18, 1116–1122 (2015).

35. S. X. Chen, A. N. Kim, A. J. Peters, T. Komiyama, Subtype-specific plasticity of inhibitory circuits in motor cortex during motor learning. Nat. Neurosci. 18, 1109–1115 (2015).

36. Y. Wang, M. Toledo-Rodriguez, A. Gupta, C. Wu, G. Silberberg, J. Luo, H. Markram, Anatomical, physiological and molecular properties of Martinotti cells in the somatosensory cortex of the juvenile rat. J. Physiol. 561, 65–90 (2004).

37. F. Crick, Function of the thalamic reticular complex: The searchlight hypothesis. Proc. Natl. Acad. Sci. U. S. A. 81, 4586–4590 (1984).

38. J. E. Lisman, Bursts as a unit of neural information: Making unreliable synapses reliable. Trends Neurosci. 20 (1997), pp. 38–43.

39. H. Markram, Y. Wang, M. Tsodyks, Differential signaling via the same axon of neocortical pyramidal neurons. Proc. Natl. Acad. Sci. U. S. A. 95, 5323–5328 (1998).

40. E. M. Izhikevich, N. S. Desai, E. C. Walcott, F. C. Hoppensteadt, Bursts as a unit of neural information: Selective communication via resonance. Trends Neurosci. 26, 161–167 (2003).

41. R. Naud, H. Sprekeler, Sparse bursts optimize information transmission in a multiplexed neural code. Proc. Natl. Acad. Sci. 115, E6329–E6338 (2018).

42. G. Doron, M. von Heimendahl, P. Schlattmann, A. R. Houweling, M. Brecht, Spiking Irregularity and Frequency Modulate the Behavioral Report of Single-Neuron Stimulation. Neuron. 81, 653–663 (2014).

43. N. Takahashi, C. Ebner, J. Sigl-Glöckner, S. Moberg, S. Nierwetberg, M. E. Larkum, Active dendritic currents gate descending cortical outputs in perception. Nat. Neurosci. 2020, 1–9 (2020).

44. D. Miyamoto, D. Hirai, C. C. A. Fung, A. Inutsuka, M. Odagawa, T. Suzuki, R. Boehringer, C. Adaikkan, C. Matsubara, N. Matsuki, T. Fukai, T. J. McHugh, A. Yamanaka, M. Murayama, Top-down cortical input during NREM sleep consolidates perceptual memory. Science. 352, 1315–1318 (2016).

45. A. Payeur, J. Guerguiev, F. Zenke, B. Richards, R. Naud, bioRxiv Neurosci., in press, doi:10.1101/2020.03.30.015511.

46. M. Larkum, A cellular mechanism for cortical associations: An organizing principle for the cerebral cortex. Trends Neurosci. 36, 141–151 (2013).

47. D. J. Felleman, D. C. Van Essen, Distributed Hierarchical Processing in the Primate Cerebral Cortex. Cereb. Cortex. 1, 1–47 (1991).

48. G. N. Ranganathan, P. F. Apostolides, M. T. Harnett, N.-L. Xu, S. Druckmann, J. C. Magee, Active dendritic integration and mixed neocortical network representations during an adaptive sensing behavior. Nat. Neurosci. (2018), doi:10.1038/s41593-018-0254-6.

49. M. Suzuki, M. E. Larkum, General Anesthesia Decouples Cortical Pyramidal Neurons. Cell. 180, 666-676 (2020).

50. G. Kreiman, T. Serre, Beyond the feedforward sweep: feedback computations in the visual cortex. Ann. N. Y. Acad. Sci. 1464, 222–241 (2020).

51. L. Madisen, T. Mao, H. Koch, J. Zhuo, A. Berenyi, S. Fujisawa, Y.-W. A. Hsu, A. J. Garcia, X. Gu, S. Zanella, J. Kidney, H. Gu, Y. Mao, B. M. Hooks, E. S. Boyden, G. Buzsáki, J. M. Ramirez, A. R. Jones, K. Svoboda, X. Han, E. E. Turner, H. Zeng, A toolbox of Cre-dependent optogenetic transgenic mice for light-induced activation and silencing. Nat. Neurosci. 15, 793–802 (2012).

52. S. Lefort, C. Tomm, J. C. Floyd Sarria, C. C. H. Petersen, The Excitatory Neuronal Network of the C2 Barrel Column in Mouse Primary Somatosensory Cortex. Neuron. 61, 301–316 (2009).

53. K. Franklin, G. Paxinos, The Mouse Brain in Stereotaxic Coordinates (Academic Press, San Diego, 2001).

54. G. Paxinos, C. Watson, The Rat Brain in Stereotaxic Coordinates (Academic Press, San Diego, 1998).

55. C. Lüscher, L. Y. Jan, M. Stoffel, R. C. Malenka, R. A. Nicoll, G protein-coupled inwardly rectifying K^+ channels (GIRKs) mediate postsynaptic but not presynaptic transmitter actions in hippocampal neurons. *Neuron*. **19**, 687–695 (1997).

56. M. V. Sanchez-Vives, A. Barbero-Castillo, M. Perez-Zabalza, R. Reig, GABAB receptors modulation of thalamocortical dynamics and synaptic plasticity. *Neuroscience* (2020), , doi:10.1016/j.neuroscience.2020.03.011.